entropy

MDPI

Article

Low Noise Opto-Electro-Mechanical Modulator for RF-to-Optical Transduction in Quantum Communications

Michele Bonaldi [1,2], Antonio Borrielli [1,2], Giovanni Di Giuseppe [3,4], Nicola Malossi [3,4], Bruno Morana [5], Riccardo Natali [3,4], Paolo Piergentili [3,4], Pasqualina Maria Sarro [5], Enrico Serra [2,5] and David Vitali [3,4,6,*]

1 Institute of Materials for Electronics and Magnetism, Nanoscience-Trento-FBK Division, 38123 Povo, TN, Italy; mbonaldi@fbk.eu (M.B.); borrielli@fbk.eu (A.B.)
2 Istituto Nazionale di Fisica Nucleare, TIFPA, 38123 Povo, TN, Italy; enrico.serra@tifpa.infn.it
3 Physics Division, School of Science and Technology, University of Camerino, 62032 Camerino, MC, Italy; gianni.digiuseppe@unicam.it (G.D.G.); nicola.malossi@unicam.it (N.M.); riccardo.natali@unicam.it (R.N.)
4 INFN, Sezione di Perugia, 06123 Perugia, PG, Italy
5 Department of Microelectronics and Computer Engineering, ECTM, Delft University of Technology, Feldmanweg 17, 2628 CT Delft, The Netherlands; b.morana@tudelft.nl (B.M.)
6 CNR-INO, L.go Enrico Fermi 6, 50125 Firenze, FI, Italy
* Correspondence: david.vitali@unicam.it; Tel.:+39-0737-402540

Abstract: In this work, we present an Opto-Electro-Mechanical Modulator (OEMM) for RF-to-optical transduction realized via an ultra-coherent nanomembrane resonator capacitively coupled to an rf injection circuit made of a microfabricated read-out able to improve the electro-optomechanical interaction. This device configuration can be embedded in a Fabry–Perot cavity for electromagnetic cooling of the LC circuit in a dilution refrigerator exploiting the opto-electro-mechanical interaction. To this aim, an optically measured steady-state frequency shift of 380 Hz was seen with a polarization voltage of 30 V and a Q-factor of the assembled device above 10^6 at room temperature. The rf-sputtered titanium nitride layer can be made superconductive to develop efficient quantum transducers.

Keywords: quantum transduction; hybrid systems; low noise N/MEMS resonators; optomechanics; electro-optics

Citation: Bonaldi, M.; Borrielli, A.; Di Giuseppe, G.; Malossi, N.; Morana, B.; Natali, R.; Piergentili, P.; Sarro, P.M.; Serra, E.; Vitali, D. Low Noise Opto-Electro-Mechanical Modulator for RF-to-Optical Transduction in Quantum Communications. *Entropy* **2023**, *25*, 1087. https://doi.org/10.3390/e25071087

Academic Editors: Rosario Lo Franco, Fabio Sciarrino and Valentina Parigi

Received: 23 June 2023
Revised: 13 July 2023
Accepted: 16 July 2023
Published: 19 July 2023

1. Introduction

Quantum transduction refers to the process of converting one form of energy to another at the single excitation level, and it represents a key ingredient in quantum technologies. Major interest is currently placed on the coherent conversion between optical and microwave/radiofrequency (mw/rf) photons [1,2], the optical domain being ideal for reliable long-range communications through optical fibers or in free space, while the lower frequency band is particularly suitable for high-fidelity local quantum operations using superconducting and other solid state processors. This will allow a global quantum Internet or distributed quantum tasks including computing or sensing [3,4]. Moreover, quantum transduction could be used for optical detection of mw/rf signals by exploiting the most efficient detectors for optical photons [5–9].

The easiest way to bridge the enormous energy gap is to use a mediator simultaneously coupled to both mw/rf and optical modes. There have been a variety of proposals using different kinds of mediating systems, including opto-electro-mechanical systems [10–17], atomic ensembles [18–21], electro-optical systems [22–27] and magnons [28].

In opto-electro-mechanical platforms, a mechanical resonator is coupled to mw/rf photons either capacitively [5–9,14–17] or via the piezoelectric effect [29–38] and dispersively via radiation pressure with the optical mode(s). Here, we shall focus on these platforms, which present a high degree of flexibility. In fact, transduction occurs at motional sidebands of the microwave and optical drivings and, depending on the detunings, one can exploit

either direct transduction with a beam-splitter-like interaction [10,11,13–15] or state transfer via quantum teleportation enabled by the microwave-optical entanglement mediated by the mechanical mode [12,39]. Moreover, by including a second mechanical mode [40–42] and by properly driving both mw/rf and optical modes with multiple tones in a phase-controlled way, one can realize nonreciprocal photon transmission/conversion [43–52]. In fact, the two mechanical modes establish two distinct paths of photon transmission which may destructively interfere, breaking the symmetry between the two directions. This has enabled the realization of isolators, circulators and directional amplifiers both at microwave [45,46,51] and at optical [48,49] frequencies, while nonreciprocal microwave-optical transducers proposed in [44,52] have not been experimentally realized yet. Typical figures of merit in quantum transduction are the conversion efficiency (or the fidelity of the transferred quantum state), the added noise and the bandwidth [53]. The two latter quantities are relevant also when transduction is exploited for sensing, as it occurs in recently demonstrated opto-electro-mechanical devices realizing optical preamplification and detection of rf signals in magnetic resonance imaging [8,9]. In these devices, the detection bandwidth of rf signals could be enhanced and engineered by again exploiting the interference between the optomechanical interaction pathways mediated by two different mechanical modes [7].

Various solutions have been adopted for the explicit design of opto-electro-mechanical transducers. In some cases, transducers are fabricated fully from a piezoelectric material, including the optomechanical cavity [29–32,35]. Other approaches exploit hybrid solutions where the optomechanical part is fabricated from Si, for example, while coupling to the microwave input is through an added piezoelectric resonator [33,34,36–38]. In these cases, quasi-resonant direct interaction between the mechanical resonator and a microwave resonator at GHz frequencies is exploited for transduction.

Electro-mechanical capacitive coupling is instead used in cases of metalized membranes [5–9,14–17] which, with an in-front electrode, may be placed within an optical Fabry–Perot cavity for radiation–pressure coupling. The metalized membrane and the electrode form a capacitor of an LC resonator whose rf photons are modulated by the membrane motion. This membrane-based geometry is used in two cases. (i) rf-optical transduction [5–9,16], in which the vibrational mode of the membrane and the LC resonator are quasi-resonant and the working point is set by an applied DC voltage bias. (ii) mw-optical transduction [14,15,17] between the fields at mechanical sideband frequencies with respect to the corresponding optical and microwave driving fields.

Here, we focus on quasi-resonant rf-optical transduction based on metalized membranes and we report a novel design of an opto-electro-mechanical modulator (OEMM) based on a resonating silicon nitride nanomembrane, which exhibits room-temperature Q-factors of 10^6 in the MHz range. Square-shaped metalized nanomembranes with the LC circuit in FR4 and quartz substrates were presented in other works with quality factors 10^5 [5,7] and resulting in more added thermal noise in the transduction scheme. Our device can be optimized to be embedded into the optical cavity for the sympathetic ground state cooling of an LC resonating circuit as proposed in [16]. We show the fundamental properties of this novel device and the fabrication process.

The paper is organised as follows. In Section 2, we describe the design strategy we have followed, while in Section 3 we provide the details of the fabrication process employed for the realization of the OEMM device. In Section 4, we provide a characterization of the electro-mechanical properties and performance of the device and in Section 5 we summarize the results and discuss the perspectives, the future research direction and potential applications.

2. Design Strategy of the OEMM

The device comprises a metal-coated silicon nitride nanomembrane that is coupled via radiation pressure to a cavity field and capacitively coupled to an rf resonant circuit via the position-dependent capacitance, as shown in Figure 1. In our design, we need to

keep the thermal noise low by providing the device with an on-chip mechanical filter for shielding the substrate's recoil losses [54]. In particular, the membrane is clamped to a hollow silicon cylinder connected with flexural joints to the two-stage shield shown in Figure 1c. The mechanical filter and the thick hollow cylinder cause the dissipation of the membrane to be dominated only by the intrinsic losses of the two films. The high stress in the membrane dilutes the loss of both films as discussed below. Moreover, the intrinsic losses of a highly stressed circular membrane are related to the dilution parameter λ, which can be expressed in terms of the aspect ratio h/R, where R is the radius and h the thickness, as $\lambda = \frac{h}{R}\sqrt{\frac{Y}{12(1-\nu^2)\sigma_0}}$, where σ_0 is the bi-axial intrinsic stress, Y the Young's modulus and ν the Poisson's ratio. The dilution parameter can be equivalently defined in terms of the flexural rigidity D of a film of a given material as $\lambda = D/(\sigma_0 h R^2)$. The intrinsic losses can be decomposed into the edge and distributed losses [55,56], which depend upon the λ parameter linearly and quadratically, respectively.

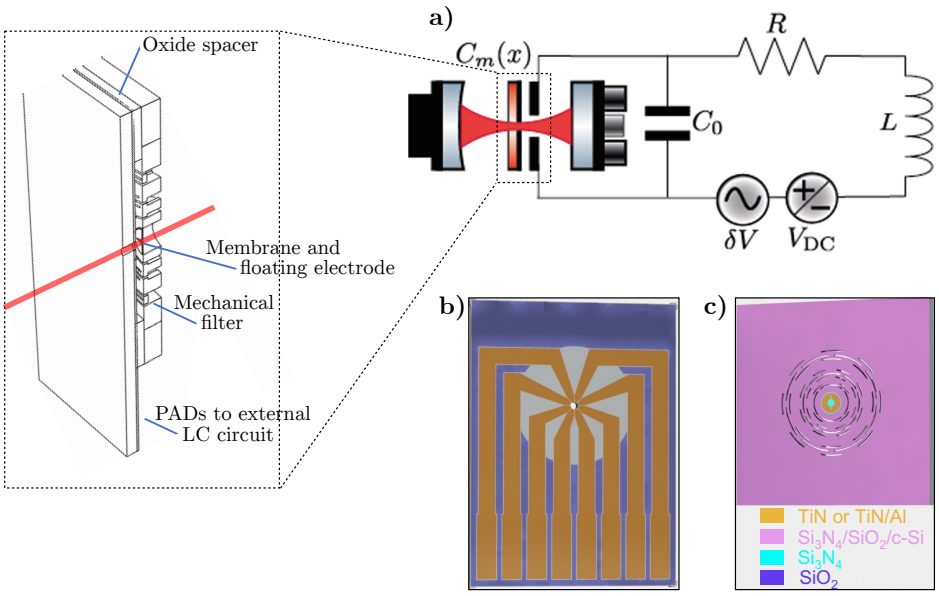

Figure 1. Opto–Electro-Mechanical Modulator. (**a**) Schematic of the setup with a detailed view of the cross-section of the OEMM embedded in the high-finesse Fabry–Perot Cavity. The rf weak δV signal is transferred to the cavity optical field after polarizing the coupling capacitor $C_m(x)$ with a DC voltage bias V_{DC}. (**b**,**c**) The two components of the OEMM device: the electrode connected to the LC circuit (**b**) and the floating electrode on the silicon nitride membrane (**c**). Materials are also specified, while the substrate is floating-zone crystalline silicon for both components.

Edge loss is due to the high curvature variations in the resonating modes in the clamping region which extends about fivefold the thickness of the SiN membrane ($5 \times h$) and affects the quality factor of the low-frequency modes. While the contribution to this loss of metal TiN coating can be easily avoided via a selective patterning of the metal film, the distributed loss degrades the overall quality factor according to the weighted sum of the bending dissipation of the two films [57]. In the following, we demonstrate that the distributed loss in the TiN coating is diluted by the tensile stress σ_0 in the SiN membrane. Starting from the definition of the quality factor of a bilayer (SiN/TiN) due to the internal bending of the films, we can write:

$$Q_{SiN/TiN} = \frac{2\pi W^t_{SiN}}{\Delta W_{SiN} + \Delta W_{TiN}} = \left(\frac{W^b_{SiN}}{W^t_{SiN}} Q^{-1}_{SiN} + \frac{W^b_{TiN}}{W^t_{SiN}} Q^{-1}_{TiN}\right)^{-1}, \quad (1)$$

where $\Delta W_{SiN}, \Delta W_{TiN}$ are the dissipated energies due to bending, while W^b_{SiN}, W^b_{TiN} are the stored bending energies of the silicon nitride film and the titanium nitride films, respectively.

W^t_{SiN} is the total tensile stored energy in the SiN film. In addition, the Q^{-1}_{SiN}, Q^{-1}_{TiN} are the intrinsic losses of the silicon nitride layer and the titanium nitride in cases of zero stress, respectively. For a circular membrane, the energy terms can be evaluated with the following formulas:

$$W^b_{SiN} = \frac{Y_{SiN}}{(1-\nu^2_{SiN})} \int_0^{2\pi} d\theta \int_{-\frac{h_{SiN}}{2}}^{\frac{h_{SiN}}{2}} z^2 dz \int_0^R \left(\frac{\partial^2 u(r)}{\partial^2 r} + \frac{1}{r}\frac{\partial u(r)}{\partial r} \right)^2 r dr\,, \tag{2}$$

$$W^b_{TiN} = \frac{Y_{TiN}}{(1-\nu^2_{TiN})} \int_0^{2\pi} d\theta \int_{\frac{h_{SiN}}{2}}^{\frac{h_{SiN}}{2}+h_{TiN}} z^2 dz \int_{R_i}^{R_e} \left(\frac{\partial^2 u(r)}{\partial^2 r} + \frac{1}{r}\frac{\partial u(r)}{\partial r} \right)^2 r dr\,, \tag{3}$$

and the tensile energy is:

$$W^t_{SiN} = \int_0^{2\pi} d\theta \int_0^R \frac{h_{SiN}\sigma_0}{2} \left(\frac{\partial u(r)}{\partial r} \right)^2 r dr\,. \tag{4}$$

Using the equation of vibrations of axisymmetric modes of a membrane under uniform tensile stress σ_0

$$\nabla_r u(r) = -\frac{\rho\omega^2}{\sigma_0} u(r) = -\Omega^2 u(r)\,, \tag{5}$$

with ρ being the membrane's density, we derive the axisymmetric solution $u_{n0}(r) = C_{0n} J_0(\alpha_{0n} r/R)$ in cases of clamped–clamped boundary conditions, where J_0 is the zero-th order Bessel function of the first kind, α_{0n} are its zeros and $\Omega_{0n} = \alpha_{0n}/R$. According to this definition, the energy terms in Equations (2) and (3) transform as

$$\begin{aligned} W^b_{SiN} &= \frac{Y_{SiN}}{(1-\nu^2_{SiN})} \int_0^{2\pi} d\theta \int_{-\frac{h_{SiN}}{2}}^{\frac{h_{SiN}}{2}} z^2 dz \int_0^R \Omega^4_{0n} C^2_{0n} J^2_0(\alpha_{0n} r/R) r dr \\ &= \pi R^2 \Omega^4_{0n} C^2_{0n} D_{SiN} J^2_1(\alpha_{n0}), \end{aligned} \tag{6}$$

$$\begin{aligned} W^b_{TiN} &= \frac{Y_{TiN}}{(1-\nu^2_{TiN})} \int_0^{2\pi} d\theta \int_{\frac{h_{SiN}}{2}}^{\frac{h_{SiN}}{2}+h_{TiN}} z^2 dz \int_{R_i}^{R_e} \Omega^4_{0n} C^2_{0n} J_0(\alpha_{0n} r/R)^2 r dr \\ &= \pi R^2 \Omega^4_{0n} C^2_{0n} D_{TiN} J_1(\alpha_{n0})^2 \left[1 - \frac{R_i^2}{R^2} \left(\frac{J_0(\alpha_{0n} R_i/R)^2}{J_1(\alpha_{0n})^2} + \frac{J_1(\alpha_{0n} R_i/R)^2}{J_1(\alpha_{0n})^2} \right) \right], \end{aligned} \tag{7}$$

where R_i, R_e are the internal and external radius of the TiN metal coating and J_1 is the first-order Bessel function of the first kind. In the above equation, without loss of generality, we assume that $R_e \simeq R$. In the fabricated device, the condition to avoid edge loss is $R_e < R$.

We now consider the tensile stored energy, which can be written starting from Equation (4) as:

$$W^t_{SiN} = \pi h_{SiN} \sigma_0 \frac{\alpha^2_{0n} C^2_{0n} J_1(\alpha_{0n})^2}{2}\,. \tag{8}$$

Using the equation above and the definition of the dilution parameter for the SiN and the TiN films given above [55], we can rewrite Equation (1) as

$$Q_{SiN/TiN} = \left(\alpha^2_{0n} \lambda^2_{SiN} Q^{-1}_{SiN} + \alpha^2_{0n} \lambda^2_{TiN} [1 - f(R_i)] Q^{-1}_{TiN} \right)^{-1}, \tag{9}$$

where:

$$f(R_i) = \frac{R_i^2}{R^2} \left(\frac{J_0(\alpha_{0n} R_i/R)^2}{J_1(\alpha_{0n})^2} + \frac{J_1(\alpha_{0n} R_i/R)^2}{J_1(\alpha_{0n})^2} \right) \tag{10}$$

is the function that modulates the distributed dissipation on the TiN film. By looking at Equation (9), the two terms represent the distributed losses for each film and show that the loss is diluted by the stress in the SiN layer. Moreover, the losses due to the TiN layer can be further reduced by increasing the $f(R_i)$ term.

The ultimate limit of the mechanical Q factor of the bilayer film is due to the edge loss ($2\lambda_{SiN}Q_{SiN}^{-1}$) in the SiN layer that must be included in Equation (1):

$$Q_{SiN/TiN}^{Tot} = \left[(2\lambda_{SiN} + \alpha_{0n}^2\lambda_{SiN}^2)Q_{SiN}^{-1} + \alpha_{0n}^2\lambda_{TiN}^2[1 - f(R_i)]Q_{TiN}^{-1}\right]^{-1}. \quad (11)$$

To the authors' knowledge, there are no data for evaluating the internal friction of the TiN coating; hence, a precise estimation of the overall Q-factor would be fair. We assume an intrinsic loss of TiN equal to 10^{-3} as usually done for simulating the effects of the metal dissipative layer. Results concerning the overall dissipation and the distribution are shown in Figure 2a for the first ten asymmetric modes by using the values reported in Table 1. The above relations demonstrate that the thickness and the shape of the metal coating on a stressed membrane can be arbitrary if patterning starts from a few microns of the membrane's edge. The distributed losses of the two films are always lower than the edge loss in the SiN layer. Similar behavior was experimentally observed in [56] where a hybrid SiN membrane with an aluminum layer was presented. The detrimental effect of the intrinsic loss of aluminum film was observed in a full-coated version of the device.

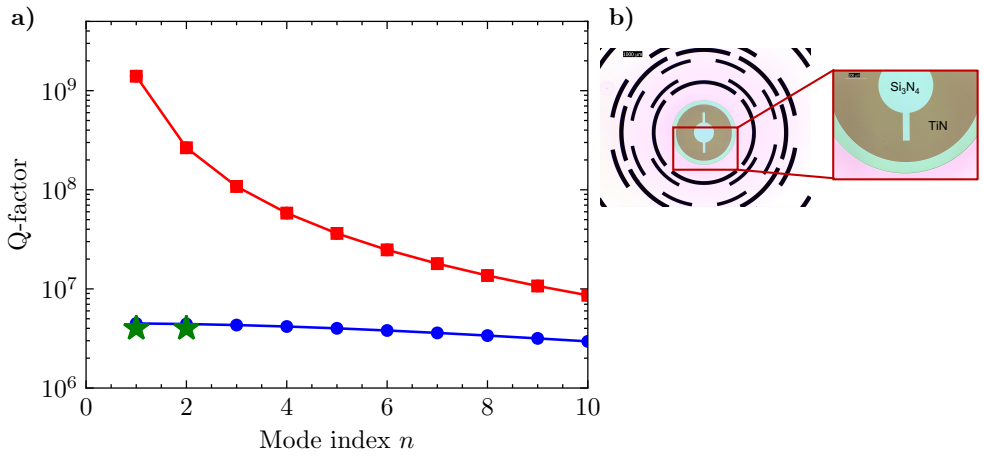

Figure 2. Dissipation of the metalized membrane. (**a**) The Q-factor of the bilayer SiN/TiN membrane without edge losses $Q_{SiN/TiN}$ (red) and with edge loss of the SiN layer $Q_{SiN/TiN}^{Tot}$ (blue). Green stars are the experimental points of the measured Q-factor for the two first axisymmetric modes with index (0,1) and (0,2). (**b**) Optical image of the SiN stoichiometric nanomembrane (light blue) with the TiN layer (brown). The membrane is endowed with the on-chip shield for recoil losses (see Ref. [54]) (right). Detailed view of the TiN notch in the membrane electrode used for the mode identification and the component assembly.

The eight-segment electrode (see Figure 1b) has been designed to satisfy the condition of constructive interference between the mechanical modes that improve the transduction of rf signals into the optical output within the frequency band between the two mechanical resonances. As described in [7], this modifies the electromagnetic coupling coefficients through the effective areas A_{eff} that are determined by the partial capacitance between the floating electrode in the membrane and the TiN/Al paths in the fixed electrode. Hence, the overall variable capacitance between two electrodes (+,−) in front of the membrane can be obtained as:

$$C_m = \left(\frac{1}{C_+} + \frac{1}{C_-}\right)^{-1}. \quad (12)$$

Assuming that the curvature of the membrane is sufficiently small so that we can take it to be locally flat:

$$C_{\pm} = \int_0^{2\pi} d\theta \int_0^R \frac{\zeta_{\pm}(r,\theta)\epsilon_0}{h_0 + \delta z(r,\theta)} r dr \,, \tag{13}$$

where h_0 is the capacitor gap, $\zeta_{\pm}(r,\theta)$ is a function that equals 1 for points in the membrane plane that are metalized and overlap with the fixed positive or negative electrode and is zero otherwise, $\delta z(r,\theta) = \sum_i \beta_i u_i(r,\theta)$ is the membrane displacement field relative to the steady-state configuration and ϵ_0 is the vacuum dielectric constant. The eight-segment electrodes were designed to maximize the capacitance variation $\frac{\partial C_{\pm}}{\partial \beta_i}$ for a given membrane's eigenmode.

Table 1. Material data for the SiN and the TiN coating. Dissipation properties at room temperature.

	SiN	**TiN**
Y [GPa]	270	600
ν	0.27	0.27
ρ [Kg/m^3]	2700	-
h [nm]	100	50
R [μm]	740	-
R_i [μm]	-	250
Q^{-1}	2.0×10^{-4}	1.0×10^{-3}

3. Fabrication of the OEMM Module

3.1. The Opto-Electro-Mechanical Resonating Part

The opto-electro-mechanical resonator is made of a Low-Pressure Chemical Vapor Deposition (LPCVD) silicon nitride (SiN) nanomembrane (100 nm nominal thickness) with a partial overlay of an rf-sputtered Titanium Nitride (TiN) deposited at 50 °C with a target thickness of 50 nm (see Figure 2b). The final thickness of the SiN membrane, measured with an ellipsometer, is (80 ± 5) nm because of several wet etching steps made by Hidrofluoridic Acid (HF) while the TiN thickness remains close to its nominal value. The nanomembrane is tensioned with a 1 GPa and insulated from the substrate by an on-chip shield where only intrinsic losses of SiN/TiN layers account for the dissipation, as discussed in Section 2. The double-stage filter is made of flexural silicon joints and masses realized on a Silicon-on-Insulator wafer with a thickness of 1 mm. To etch silicon, we used a double-side bulk micromachining Inductive Coupled Plasma–Deep Reactive Ion Etching (ICP-DRIE) Bosch recipe. Descriptions of similar devices with the fabrication steps can be found in [54,55,58].

3.2. Microfabricated Coupling Capacitor

The LC circuit for the injection of the rf signal is made of an external capacitance, inductance and a microfabricated electromechanical coupling capacitor. The target armature distance between the membrane and the eight-segment electrode must be lower than 10 μm. The surface/bulk-micromachining double-side microfabrication process was developed starting from a high resistivity p-type Si wafer with <100> orientation, 100 mm diameter and thickness of 1 mm. The principal process steps are shown in Figure 3.

Fabrication starts by thermally growing 500 nm thick oxide for the electrical insulation of the metal paths. The TiN/Al stacks were rf-sputtered with target thicknesses of 50 nm/500 nm, respectively. A plasma etching of the TiN/Al stack was done by using an inductively coupled plasma machine based on Ar/CHF_3 chemistry and landing on the thermal oxide layer (see steps 1–2 in Figure 3).

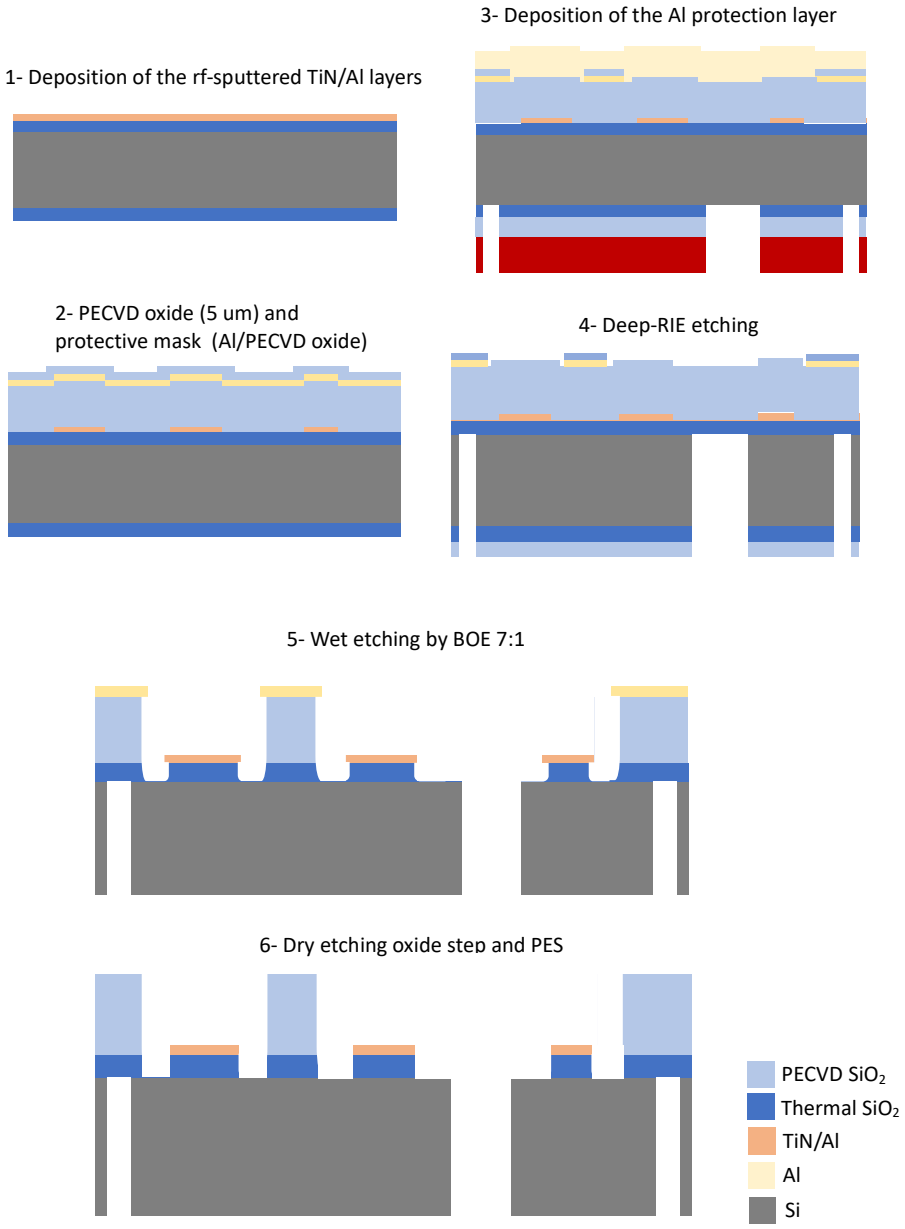

Figure 3. Main steps of the microfabrication process flow-chart.

Deposition of 5 µm thick PECVD TEOS oxide on top of the Si substrate that covers the metal paths was used as the etch stop layer for the ICP-DRIE etching. The through-holes have a target diameter of 500 µm. The PECVD TEOS oxide works also as a spacer for the OEMM component assembly. The oxide spacer was patterned to open the interaction area (corresponding to the filter region) and the trenches between the eight-segment electrode. This step was done using an extra mask layer made of Al/PECVD oxide on the top of the substrate (see steps 2–3 in Figure 3). After this step, an aluminum capping layer was deposited on the top side for thermalization for the through-wafer silicon etching step. The bottom side was prepared with 4 µm PECVD oxide for the Si etching. Deep-RIE Bosch plasma etchings with SF_6 and C_4F_8 as etching and passivation gasses, respectively, were done in an inductive plasma machine for the definition of the through-hole and the dicing lines. Each device is supported on the four corners by silicon beams (width 500 µm) connecting the device with the wafer for subsequent manual dicing (see steps in 3–4 Figure 3).

A BOE (buffered oxide etch) 1:7 was carried out on each device to remove the PECVD oxide (see step 5 in Figure 3) around the Al mask and TiN/Al layer. The first mask protects the PECVD oxide spacer, and the second the insulation thermal oxide. After BOE 1:7, the Al stripping was done with PES-77-19-04, which mainly consists of phosphoric acid (H_3PO_4). In fact, PES can be a mixture 1–5% HNO_3 (for Al oxidation), 65–75% H_3PO_4 (to dissolve the Al_2O_3), 5–10% CH_3COOH (for wetting and buffering) and H_2O dilution to define the etch rate at a given temperature. There is a <1 µm undercut on the sidewall of the TiN/Al/SiO_2 oxide. The minimum distance between the metal paths and the oxide spacer is 50 µm while the distance from the central hole is 30 µm. Dry etching was performed with a plasma machine to remove unwanted extra oxide layers between the metal paths exploiting the selectivity of the TiN metallization with respect to oxide (see step 6 in Figure 3). The TiN layer was used also because it is inerted in most chemical baths and simplifies microfabrication. The PECVD oxide spacer has a final thickness of 1.1 µm. The cleaning was done with an ultrasonic bath and a custom Teflon holder inside a glass beaker heated by a hot plate. Devices are positioned to facilitate the bubbling of hot 60 °C DI water and a pipe for the continuous replacement of the exhausted DI water.

3.3. OEMM Assembly Procedure

The alignment is performed on a custom designed Teflon support in which references have been integrated in the eight-segment chip. The alignment system is mounted on a crystallographic microscope and centering is done manually using as a reference the notch on the TiN electrode on the membrane and the space between two metal tracks in the fixed electrode chip. A membrane/electrode alignment precision on the plane of less than 35 µm Figure 4 was estimated, which was in line with that of machines performing chip-to-chip bonding. The two chips are glued by the Stycast 2850 FT glue for cryogenic applications and applied to three device edges. Weights are placed on top of the upper chip to avoid that the glue spills into the internal region of the device, increasing the capacitor gap. The assembled OEMM device was finally glued to an oxygen-free high thermal conductivity (OFHC) copper plate for thermalization and connected to the PCB auxiliary element with Ag paste; see Figure 4 (right).

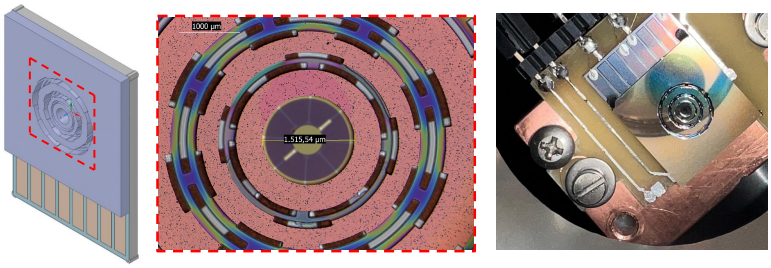

Figure 4. Detailed view of the interaction region in the OEMM assembled device (**left**). The OEMMs clamped to the OFHC copper block (**center**) and the diving PCB board used in the optical setup (**right**).

4. Characterization

4.1. Modal Analysis of the OEMMs

The modal frequencies and the quality factors of the mechanical oscillator are measured by means of an interferometric technique with shot-noise limited homodyne detection. The setup is shown in Figure 5 and the measurement techniques are discussed in [7]. In Figure 6a the voltage noise spectrum of the homodyne signal at the output of the interferometer is presented. The resonances are related to the peaks of the voltage noise spectrum emerging from the background shot noise.

The modal frequencies and modal indexes are derived from a Finite Element Method (FEM) simulation of the eigenfrequencies of a SiN membrane with the TiN layer under tensile stress. Data used in the simulation are presented in Table 1. We note that the relative error R_E between the experimental results and those of the simulation is always below

3%, as reported in Table 2. In Figure 6b the simulated modal shape functions of the first nine modes are reported. The degenerate modes are split in frequency depending on the fabrication irregularities (hole eccentricity) and the presence of the TiN layer. Modes with moving mass in the central hole of the membrane are close to those of circular membranes, but the two-fold degeneracy is split in frequency.

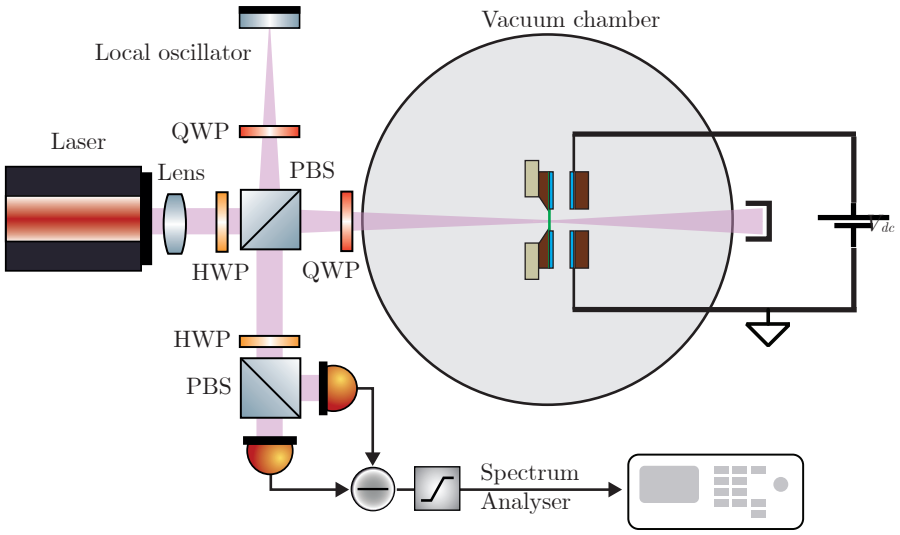

Figure 5. Experimental setup. Michelson interferometer with shot-noise limited homodyne detection.

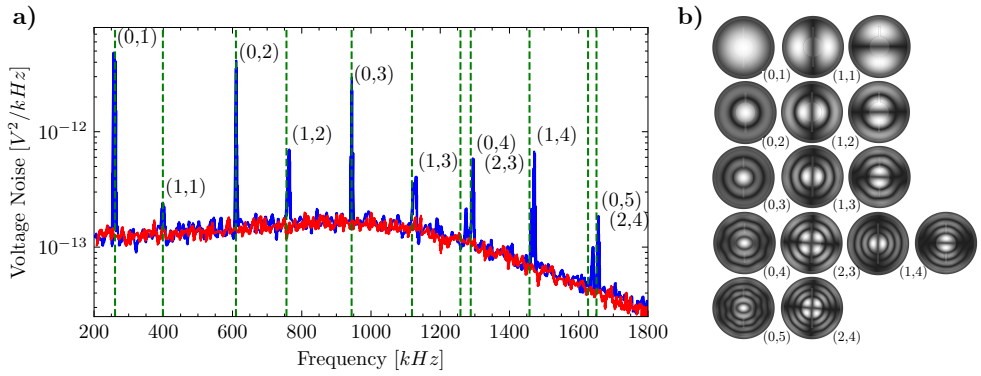

Figure 6. Mechanical mode characterization. (**a**) Voltage spectral noise of the homodyne signal (blue) and the shot-noise contribution (red). Mechanical modes of the functionalized Si_3N_4 membrane correspondence to the peaks of the spectrum. The first mode has frequency $f_{(0,1)} = 260.65$ kHz. The green dashed lines are the calculated frequencies from the FEM simulation. (**b**) Calculated mode shapes via FEM simulation, corresponding to the calculated mode frequencies present in the spectrum. Axisymmetric modes and modes with two-fold degeneracy are classified according to the number of nodal and circumference indexes. Frequency increases from the top to the bottom and from left to right.

The characterization of the quality factor was performed by the ring-down technique. The mechanical oscillator is excited on-resonance by a piezoelectric element and then left to relax in order to measure the amplitude decay time. In Figure 7, we present the mechanical Q-factor measurements for the assembled device in the frequency range [200 kHz, 1 MHz], while in the inset we present the ring-down measurement for the mode (0,1). The ring down measurement signal is given by the voltage spectral noise density (VSN) of the homodyne detection signal, measured by a spectrum analyzer, during the excitation–dexcitation cycle of the mechanical oscillator mode. The overall Q-factor at room temperature after the assembling procedure is still of the order of 10^6, which is compatible for the foreseen application of the system [16].

Table 2. Measured and computed FEM of the detected eigenfrequencies of the OEMM membrane resonator. The corresponding shape functions are represented in Figure 6b.

Mode Index	f^{FEM} [kHz]	f^{meas} [kHz]	$\lvert R_E \rvert$%
(0,1)	260.645	258.786	0.718
(1,1)	398.802	399.587	0.196
(0,2)	609.854	611.659	0.295
(1,2)	755.813	764.629	1.153
(0,3)	943.985	943.094	0.094
(1,3)	1118.259	1129.09	0.959
(0,4)	1258.374	1296.55	2.944
(2,3)	1288.075	1275.69	0.971
(1,4)	1457.844	1471.24	0.910
(0,5)	1626.986	1640.15	0.802
(2,4)	1651.324	1658.11	0.409

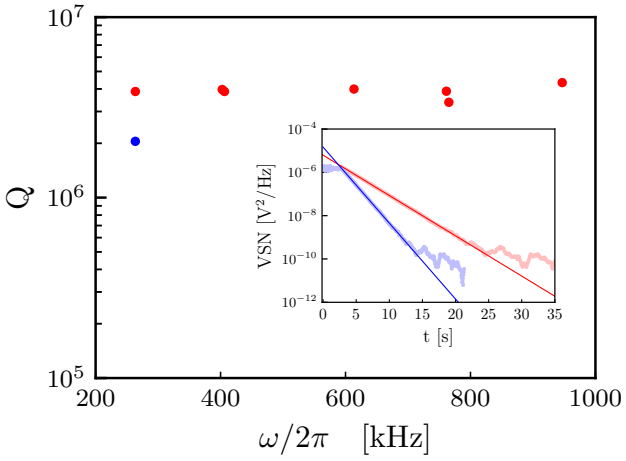

Figure 7. Measurement of the mechanical Q-factor for different modes after the final assembling of the device. Red points correspond to measurements at V_{DC} = 0 V, the blue point corresponds to the measurement at V_{DC} = 30 V. Inset: voltage spectral noise (VSN) density of the homodyne signal during the ring-down measurement of the fundamental mode (0,1) at V_{DC} = 0 V (dotted red line) and V_{DC} = 30 V (dotted blue line) and corresponding fit (continuous lines), with best fit values $\tau_{0V} = 4.668 \pm 0.008$ s and $\tau_{30V} = 2.476 \pm 0.004$ s, respectively.

We also investigate the effect of the electro-mechanical coupling on the quality factor of the mechanical resonator. In Figure 7, we present the measurement of the quality factor of the mode (0,1) at $V_{dc} = 30$ V (blue dot) via the ring-down technique (inset). The measured decrease in the quality factor may be connected to the membrane tension change due to the presence of the electrostatic force and a further systematic investigation of this effect is planned in future developments.

4.2. Electro–Mechanical Characterization of OEMM Device

In order to characterize the electromechanical properties of the device, we now consider the coupling effect induced by a DC voltage bias, V_{DC}, applied to the device electrodes, which induces a linear capacitive coupling between the electrical and mechanical system [5,7,16]. The electro-mechanical coupling induces a static shift in the mechanical frequency, caused by the electrostatic force, arising between the metalized membrane surface and the electrodes, like the force arising between the plates of a capacitor. For a capacitively-coupled system, the angular frequency shift is given by [5]:

$$\Delta\Omega_m = -\frac{d^2C(x)}{dx^2}\frac{V_{DC}^2}{2m\Omega_m} \tag{14}$$

where $C(x)$ is the capacitance of the electrode/membrane capacitor, x is the position of the mechanical oscillator (the membrane), m is the mass of the oscillator, Ω_m is the unperturbed mechanical angular frequency and V_{DC} is the applied voltage. As shown in [7,16], the frequency shift can be written as a function of the geometrical parameter of the device as follows:

$$\Delta f_m = -\frac{\epsilon_0}{8\pi^2}\frac{A_{eff}}{m_{eff}d^3 f_0}V_{DC}^2\,, \tag{15}$$

where ϵ_0 is the vacuum electrical permittivity, d the average distance between the electrodes and the membrane, A_{eff} the overlapping area between the electrode and the membrane, weighted by the mechanical mode shape, m_{eff} the mechanical oscillator mass and f_0 the unperturbed mechanical oscillator mode frequency.

In Figure 8, we show the measurement of the frequency shift of the mode (1,1) as a function of the voltage V_{DC}, which is applied to two electrodes that are symmetric with respect to the nodal axis of the (1,1) mode. We estimated the average distance between the electrodes and the membrane to be $d = (5.12 \pm 0.14)$ µm, by fitting the data with Equation (15) and by using the following parameters: effective area $A_{eff} = 0.075$ mm^2; membrane mass $m_{eff} = 420$ ng; measured unperturbed mode frequency $f_0 = f_{11} =$ 399,587 Hz.

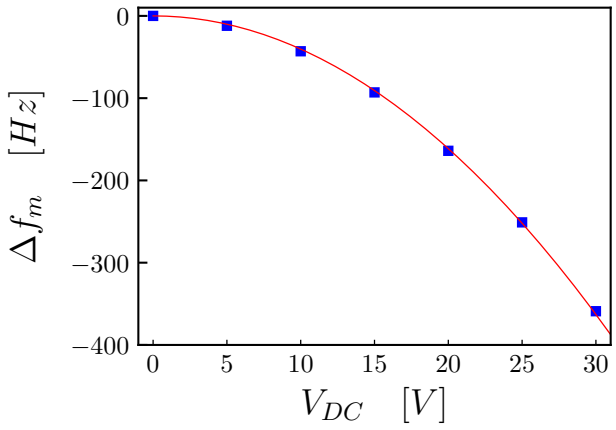

Figure 8. Measurement of the frequency shift of the (1,1) mode as a function of the DC voltage bias V_{DC} (blue square). The red line is the fit of the data using Equation (15), with best value of the average distance between the electrodes and the membrane of $d = (5.12 \pm 0.14)$ µm and using the following parameters: effective area $A_{eff} = 0.075$ mm^2; membrane mass $m_{eff} = 420$ ng; measured unperturbed mode frequency $f_0 = f_{11} = 399{,}587$ Hz.

5. Discussion and Future Perspectives

In this work, we present a membrane-based ultra-coherent OEMM that is potentially able to realize the bidirectional transduction of weak signals between the MHz domain into the THz (optical) domain. This kind of devices could be employed for the transduction of quantum signals at the input and output of solid-state superconducting processors, usually operated at rf/microwave frequencies, to optical fiber connections which are suitable for long distance quantum communication [2–4]. The same transduction could be useful for quantum sensing because weak rf signals could be read by means of easily available quantum limited optical photodetectors [9]. This signal transduction can be applied to both discrete and continuous variable degrees of freedom of the radiation field and therefore to different scenarios of quantum information encoding. In this respect, the sympathetic ground-state cooling of an LC resonator in a dilution refrigerator could be an important step for the realization of these quantum transducers [16]. Innovative materials are also tested. For instance, the rf-sputtered TiN layers were used for the first time as electrodes in OEMMs with the aim of exploiting the superconductive properties to effectively cool the mechanical

mode. Our OEMM design takes advantage of the fact that the Q-factor is independent of mounting even at the level of the membrane because the two-stage filter works as a shield for the substrate modes originating from the vibration of the coupling electrode, which is clamped to the holder in the cryogenic/vacuum chamber. This configuration is comparable to other state-of-the-art devices developed by other groups, with a good reliability but with potentially higher mechanical Q-factors and together with a wide bandwidth even in the presence of large DC biases.

Author Contributions: Conceptualization, M.B., A.B., N.M., E.S., R.N. and D.V.; methodology, M.B., A.B., N.M., B.M., E.S., R.N., P.P. and D.V.; validation, A.B., G.D.G., N.M., B.M., R.N., P.P., P.M.S. and E.S.; formal analysis, M.B., E.S., N.M., P.P. and D.V.; writing—original draft preparation, G.D.G., E.S., N.M., P.P. and D.V.; writing—review and editing, M.B., A.B., G.D.G., P.M.S., N.M., P.P. and D.V.; funding acquisition, E.S. and D.V. All authors have read and agreed to the published version of the manuscript.

Funding: This research was funded by internal resources of the INFN tHEEOM-RD experiment.

Institutional Review Board Statement: Not applicable.

Data Availability Statement: Not applicable.

Acknowledgments: We acknowledge the support of PNRR MUR project PE0000023-NQSTI (Italy).

Conflicts of Interest: The authors declare no conflict of interest.

Abbreviations

The following abbreviations are used in this manuscript:

OEMM	Opto-Electro-Mechanical-Modulator
FEM	Finite Element Method

References

1. Chu, Y.; Gröblacher, S. A perspective on hybrid quantum opto- and electromechanical systems. *Appl. Phys. Lett.* **2020**, *117*, 150503. [CrossRef]
2. Lauk, N.; Sinclair, N.; Barzanjeh, S.; Covey, J.P.; Saffman, M.; Spiropulu, M.; Simon C. Perspectives on quantum transduction. *Quantum Sci. Technol.* **2020**, *5*, 020501. [CrossRef]
3. Kimble, H.J. The quantum Internet. *Nature* **2008**, *453*, 1023–1030. [CrossRef]
4. Pirandola, S.; Bardhan, B.R.; Gehring, T.; Weedbrook, C.; Lloyd, S. Advances in photonic quantum sensing. *Nat. Photon.* **2018**, *12*, 724–733. [CrossRef]
5. Bagci, T.; Simonsen, A.; Schmid, S.; Villanueva, L.G.; Zeuthen, E.; Appel, J.; Taylor, J.M.; Sørensen, A.; Usami, K.; Schliesser, A.; et al. Optical detection of radio waves through a nanomechanical transducer. *Nature* **2014**, *507*, 81–85. [CrossRef] [PubMed]
6. Takeda, K.; Nagasaka, K.; Noguchi, A.; Yamazaki, R.; Nakamura, Y.; Iwase, E.; Taylor, J.M.; Usami, K. Electro-mechano-optical detection of nuclear magnetic resonance. *Optica* **2018**, *5*, 152–158. [CrossRef]
7. Moaddel Haghighi, I.; Malossi, N.; Natali, R.; Di Giuseppe, G.; Vitali, D. Sensitivity-Bandwidth Limit in a Multimode Optoelectromechanical Transducer. *Phys. Rev. Appl.* **2018**, *9*, 034031. [CrossRef]
8. Simonsen, A.; Saarinen, S.A.; Sánchez-Heredia, J.D.; Ardenkjær-Larsen, J.H.; Schliesser, A.; Polzik, E.S. Sensitive optomechanical transduction of electric and magnetic signals to the optical domain. *Opt. Express* **2019**, *27*, 18561. [CrossRef]
9. Simonsen, A.; Sánchez-Heredia, J.D.; Saarinen, S.A.; Ardenkjær-Larsen, J.H.; Schliesser A.; Polzik, E.S. Magnetic resonance imaging with optical preamplication and detection. *Sci. Rep.* **2019**, *9*, 18173. [CrossRef]
10. Wang, Y.-D.; Clerk, A.A. Using Interference for High Fidelity Quantum State Transfer in Optomechanics. *Phys. Rev. Lett.* **2012**, *108*, 153603. [CrossRef]
11. Tian, L. Adiabatic State Conversion and Pulse Transmission in Optomechanical Systems. *Phys. Rev. Lett.* **2012**, *108*, 153604. [CrossRef] [PubMed]
12. Barzanjeh, S.; Abdi, M.; Milburn, G.J.; Tombesi, P.; Vitali, D. Reversible Optical-to-Microwave Quantum Interface. *Phys. Rev. Lett.* **2012**, *109*, 130503. [CrossRef] [PubMed]
13. Hill, J.T.; Safavi-Naeini, A.H.; Chan, J.; Painter, O. Coherent optical wavelength conversion via cavity optomechanics. *Nat. Commun.* **2010**, *3*, 1196. [CrossRef]
14. Andrews, R.W.; Peterson, R.W.; Purdy, T.P.; Cicak, K.; Simmonds, R.W.; Regal, C.A.; Lehnert, K.W. Bidirectional and efficient conversion between microwave and optical light. *Nat. Phys.* **2014**, *10*, 321–326. [CrossRef]

15. Higginbotham, A.P.; Burns, P.S.; Urmey, M.D.; Peterson, R.W.; Kampel, N.S.; Brubaker, B.M.; Smith, G.; Lehnert, K.W.; Regal, C.A. Harnessing electro-optic correlations in an efficient mechanical converter. *Nat. Phys.* **2018**, *14*, 1038–1042. [CrossRef]
16. Malossi, N.; Piergentili, P.; Li, J.; Serra, E.; Natali, R.; Di Giuseppe, G.; Vitali, D. Sympathetic cooling of a radio-frequency LC circuit to its ground state in an optoelectromechanical system. *Phys. Rev. A* **2021**, *103*, 033516. [CrossRef]
17. Brubaker, B.M.; Kindem, J.M.; Urmey, M.D.; Mittal, S.; Delaney, R.D.; Burns, P.S.; Vissers, M.R.; Lehnert, K.W.; Regal, C.A. Optomechanical ground-state cooling in a continuous and efficient electro-optic transducer. *Phys. Rev. X* **2022**, *12*, 021062. [CrossRef]
18. Hafezi, M.; Kim, Z.; Rolston, S.L.; Orozco, L.A.; Lev, B.L.; Taylor, J.M. Atomic interface between microwave and optical photons. *Phys. Rev. A* **2012**, *85*, 020302. [CrossRef]
19. Petrosyan, D.; Mølmer, K.; Fortágh, J.; Saffman, M. Microwave to optical conversion with atoms on a superconducting chip. *New J. Phys.* **2019**, *21*, 073033. [CrossRef]
20. Tu, H.-T.; Liao, K.-Y.; Zhang, Z.-X.; Liu, X.-H.; Zheng, S.-Y.; Yang, S.-Z.; Zhang, X.-D.; Yan, H.; Zhu, S.-L. High-efficiency coherent microwave-to-optics conversion via off-resonant scattering. *Nat. Photon.* **2022**,*16*, 291–296. [CrossRef]
21. Kumar, A.; Suleymanzade, A.; Stone, M.; Taneja, L.; Anferov, A.; Schuster, D.I.; Simon J. Quantum-enabled millimetre wave to optical transduction using neutral atoms. *Nature* **2023**, *615*, 614–619. [CrossRef]
22. Tsang, M. Cavity quantum electro-optics. *Phys. Rev. A* **2010**, *81*, 063837. [CrossRef]
23. Rueda, A.; Hease, W.; Barzanjeh, S.; Fink, J.M. Electro-optic entanglement source for microwave to telecom quantum state transfer. *Npj Quantum Inf.* **2019**, *5*, 108. [CrossRef]
24. McKenna, T.P.; Witmer, J.D.; Patel, R.N.; Jiang, W.; Van Laer, R.; Arrangoiz-Arriola, P.; Wollack, E.A.; Herrmann, J.F.; Safavi-Naeini, A.H. Cryogenic microwave-to-optical conversion using a triply resonant lithium-niobate-on-sapphire transducer. *Optica* **2020**, *7*, 1737–1745. [CrossRef]
25. Hease, W.; Rueda, A.; Sahu, R.; Wulf, M.; Arnold, G.; Schwefel, H.G.L.; Fink, J.M. Bidirectional Electro-Optic Wavelength Conversion in the Quantum Ground State. *PRX Quantum* **2020**, *1*, 020315. [CrossRef]
26. Sahu, R.; Hease, W.; Rueda, A.; Arnold, G.; Qiu, L.; Fink, J.M. Quantum-enabled operation of a microwave-optical interface. *Nat. Commun.* **2022**, *13*, 1276. [CrossRef]
27. Sahu, R.; Qiu, L.; Hease, W.; Arnold, G.; Minoguchi, Y.; Rabl, P.; Fink, J.M. Entangling microwaves with light. *Science* **2023**, *380*, 718–721. [CrossRef]
28. Hisatomi, R.; Osada, A.; Tabuchi, Y.; Ishikawa, T.; Noguchi, A.; Yamazaki, R.; Usami, K.; Nakamura, Y. Bidirectional conversion between microwave and light via ferromagnetic magnons. *Phys. Rev. B* **2016**, *93*, 174427. [CrossRef]
29. Vainsencher, A.; Satzinger, K.J.; Peairs, G.A.; Cleland, A.N. Bi-directional conversion between microwave and optical frequencies in a piezoelectric optomechanical device. *Appl. Phys. Lett.* **2016**, *109*, 033107. [CrossRef]
30. Balram, K.C.; Davanco, M.I.; Song, J.D.; Srinivasan, K. Coherent coupling between radiofrequency, optical and acoustic waves in piezo-optomechanical circuits. *Nat. Photon.* **2016**, *10*, 346–352. [CrossRef]
31. Schneider, K.; Baumgartner, Y.; Hönl, S.; Welter, P.; Hahn, H.; Wilson, D.J.; Czornomaz, L.; Seidler, P. Optomechanics with one-dimensional gallium phosphide photonic crystal cavities. *Optica* **2019**, *6*, 577–584. [CrossRef]
32. Stockill, R.; Forsch, M.; Hijazi, F.; Beaudoin, G.; Pantzas, K.; Sagnes, I.; Braive, R.; Gröblacher, S. Ultra-low-noise Microwave to Optics Conversion in Gallium Phosphide. *Nat. Commun.* **2022**, *13*, 6583. [CrossRef] [PubMed]
33. Jiang, W.; Patel, R.N.; Mayor, F.M.; McKenna, T.P.; Arrangoiz-Arriola, P.; Sarabalis, C.J.; Witmer, J.D.; Laer, R.V.; Safavi-Naeini, A.H. Lithium niobate piezo-optomechanical crystals. *Optica* **2019**, *6*, 845–853. [CrossRef]
34. Shao, L.; Yu, M.; Maity, S.; Sinclair, N.; Zheng, L.; Chia, C.; Shams-Ansari, A.; Wang, C.; Zhang, M.; Lai, K.; et al. Microwave-to-optical conversion using lithium niobate thin-film acoustic resonators. *Optica* **2019**, *6*, 1498–1505. [CrossRef]
35. Jiang, W.; Sarabalis, C.J.; Dahmani, Y.D.; Patel, R.N.; Mayor, F.M.; McKenna, T.P.; Van Laer, R.; Safavi-Naeini, A.H. Efficient bidirectional piezo-optomechanical transduction between microwave and optical frequency. *Nat. Commun.* **2020**, *11*, 1166. [CrossRef] [PubMed]
36. Han, X.; Fu, W.; Zhong, C.; Zou, C.-L.; Xu, Y.; Sayem, A.A.; Xu, M.; Wang, S.; Cheng, R.; Jiang, L.; et al. Cavity piezo-mechanics for superconducting-nanophotonic quantum interface. *Nat. Commun.* **2020**, *11*, 3237. [CrossRef] [PubMed]
37. Forsch, M.; Stockill, R.; Wallucks, A.; Marinkovic, I.; Gärtner, C.; Norte, R.A.; van Otten, F.; Fiore, A.; Srinivasan, K.; Gröblacher, S. Microwave-to-optics conversion using a mechanical oscillator in its quantum ground state. *Nat. Phys.* **2020**, *16*, 69–74. [CrossRef]
38. Mirhosseini, M.; Sipahigil, A.; Kalaee, M.; Painter, O. Superconducting qubit to optical photon transduction. *Nature* **2020**, *588*, 599–603. [CrossRef]
39. Zhong, C.; Wang, Z.; Zou, C.; Zhang, M.; Han, X.; Fu, W.; Xu, M.; Shankar, S.; Devoret, M.H.; Tang, H.X.; et al. Proposal for Heralded Generation and Detection of Entangled Microwave–Optical-Photon Pairs. *Phys. Rev. Lett.* **2020**, *124*, 010511. [CrossRef]
40. Piergentili, P.; Catalini, L.; Bawaj, M.; Zippilli, S.; Malossi, N.; Natali, R.; Vitali, D.; Di Giuseppe, G. Two-membrane cavity optomechanics. *New J. Phys.* **2018**, *20*, 083024. [CrossRef]
41. Piergentili, P.; Li, W.; Natali, R.; Malossi, N.; Vitali, D.; Di Giuseppe, G. Two–membrane cavity optomechanics: Non–linear dynamics. *New J. Phys.* **2021**, *7*, 073013. [CrossRef]
42. Piergentili, P.; Li, W.; Natali, R.; Malossi, N.; Vitali, D.; Di Giuseppe, G. Absolute Determination of the Single-Photon Optomechanical Coupling Rate via a Hopf Bifurcation. *Phys. Rev. Appl.* **2021**, *15*, 034012. [CrossRef]

43. Metelmann, A.; Clerk, A.A. Nonreciprocal Photon Transmission and Amplification via Reservoir Engineering. *Phys. Rev. X* **2015**, *5*, 021025. [CrossRef]
44. Xu, X.-W.; Li, Y.; Chen, A.-X.; Liu, Y.-X. Nonreciprocal conversion between microwave and optical photons in electro-optomechanical systems. *Phys. Rev. A* **2016**, *93*, 023827. [CrossRef]
45. Bernier, N.R.; Tòth, L.D.; Koottandavida, A.; Ioannou, M.A.; Malz, D.; Nunnenkamp, A.; Feofanov, A.K.; Kippenberg, T.J. Nonreciprocal reconfigurable microwave optomechanical circuit. *Nat. Commun.* **2017**, *8*, 604. [CrossRef]
46. Barzanjeh, S.; Wulf, M.; Peruzzo, M.; Kalaee, M.; Dieterle, P.B.; Painter, O.; Fink, J.M. Mechanical on-chip microwave circulator. *Nat. Commun.* **2017**, *8*, 953. [CrossRef]
47. Miri, M.-A.; Ruesink, F.; Verhagen, E.; Alù, A. Optical Nonreciprocity Based on Optomechanical Coupling. *Phys. Rev. Appl.* **2017**, *7*, 064014. [CrossRef]
48. Shen, Z.; Zhang, Y.-L.; Chen, Y.; Sun, F.-W.; Zou, X.-B.; Guo, G.-C.; Zou, C.-L.; Dong, C.-H. Reconfigurable optomechanical circulator and directional amplifier. *Nat. Commun.* **2018**, *9*, 1797. [CrossRef]
49. Ruesink, F.; Mathew, J.P.; Miri, M.-A.; Alù, A.; Verhagen, E. Optical circulation in a multimode optomechanical resonator. *Nat. Commun.* **2018**, *9*, 1798. [CrossRef]
50. Malz, D.; Tòth, L.D.; Bernier, N.R.; Feofanov, A.K.; Kippenberg, T.J.; Nunnenkamp, A. Quantum-Limited Directional Amplifiers with Optomechanics. *Phys. Rev. Lett.* **2018**, *120*, 023601. [CrossRef]
51. Mercier de Lèpinay, L.; Ockeloen-Korppi, C.F.; Malz, D.; Sillanpää, M.A. Nonreciprocal Transport Based on Cavity Floquet Modes in Optomechanics. *Phys. Rev. Lett.* **2020**, *125*, 023603. [CrossRef] [PubMed]
52. Eshaqi-Sani, N.; Zippilli, S.; Vitali, D. Nonreciprocal conversion between radio-frequency and optical photons with an optoelectromechanical system. *Phys. Rev. A* **2022**, *106*, 032606. [CrossRef]
53. Zeuthen, E.; Schliesser, A.; Sørensen, A.S.; Taylor, J.M. Figures of merit for quantum transducers. *Quantum Sci. Technol.* **2020**, *5*, 034009. [CrossRef]
54. Borrielli, A.; Marconi, L.; Marin, F.; Marino, F.; Morana, B.; Pandraud, G.; Pontin, A.; Prodi, G.A.; Sarro, P.M.; Serra, E.; et al. Control of recoil losses in nanomechanical SiN membrane resonators. *Phys. Rev. B* **2016**, *94*, 121403(R). [CrossRef]
55. Serra, E.; Borrielli, A.; Marin, F.; Marino, F.; Malossi, N.; Morana, B.; Piergentili, P.; Prodi, G.A.; Sarro, P.M.; Vezio, P.; et al. Silicon-nitride nanosensors toward room temperature quantum optomechanics. *J. App. Phys.* **2021**, *130*, 064503. [CrossRef]
56. Yu, P.-L.; Purdy, T.P.; Regal, C.A. Control of Material Damping in High-Q Membrane Microresonators. *Phys. Rev. Lett.* **2012**, *108*, 083603. [CrossRef]
57. Sosale, G.; Prabhakar, S.; Frechette, L.G.; Vengallatore, S. A Microcantilever Platform for Measuring Internal Friction in Thin Films Using Thermoelastic Damping for Calibration. *J. Microelectromech. Syst.* **2011**, *20*, 764–773. [CrossRef]
58. Serra, E.; Morana, B.; Borrielli, A.; Marin, F.; Pandraud, G.; Pontin, A.; Prodi, G.A.; Sarro, P.M.; Bonaldi, M. Silicon Nitride MOMS Oscillator for Room Temperature Quantum Optomechanics. *J. Microelectromech. Syst.* **2018**, *26*, 1193–1203. [CrossRef]